Front. Phys. 13(3), 138501 (2018)
https://doi.org/10.1007/s11467-018-0750-x

RESEARCH ARTICLE

First-principles investigation of quantum transport in GeP_3 nanoribbon-based tunneling junctions

Qiang Wang[1,2], Jian-Wei Li[2], Bin Wang[2,†], Yi-Hang Nie[1,3,‡]

[1] *Institute of Theoretical Physics and Department of Physics, Shanxi University, Taiyuan 030006, China*
[2] *Shenzhen Key Laboratory of Advanced Thin Films and Applications, College of Physics and Energy, Shenzhen University, Shenzhen 518060, China*
[3] *State Key Laboratory of Quantum Optics and Quantum Optics Devices, Institute of Opto-Electronics, Shanxi University, Taiyuan 030006, China*
Corresponding authors. E-mail: †*binwang@szu.edu.cn*, ‡*nieyh@sxu.edu.cn*
Received November 8, 2017; accepted December 27, 2017

Two-dimensional (2D) GeP_3 has recently been theoretically proposed as a new low-dimensional material [*Nano Lett.* 17(3), 1833 (2017)]. In this manuscript, we propose a first-principles calculation to investigate the quantum transport properties of several GeP_3 nanoribbon-based atomic tunneling junctions. Numerical results indicate that monolayer GeP_3 nanoribbons show semiconducting behavior, whereas trilayer GeP_3 nanoribbons express metallic behavior owing to the strong interaction between each of the layers. This behavior is in accordance with that proposed in two-dimensional GeP_3 layers. The transmission coefficient $T(E)$ of tunneling junctions is sensitive to the connecting formation between the central monolayer GeP_3 nanoribbon and the trilayer GeP_3 nanoribbon at both ends. The $T(E)$ value of the bottom-connecting tunneling junction is considerably larger than those of the middle-connecting and top-connecting ones. With increases in gate voltage, the conductances increase for the bottom-connecting and middle-connecting tunneling junctions, but decrease for the top-connecting tunneling junctions. In addition, the conductance decreases exponentially with respect to the length of the central monolayer GeP_3 nanoribbon for all the tunneling junctions. I–V curves show approximately linear behavior for the bottom-connecting and middle-connecting structures, but exhibit negative differential resistance for the top-connecting structures. The physics of each phenomenon is analyzed in detail.

Keywords quantum transport, GeP_3 tunneling junctions, NEGF-DFT

PACS numbers 85.35.-p, 73.63.-b, 71.15.Mb

1 Introduction

Since fabrication of graphene in 2004 by Giem *et al.* in experiment [2], two-dimensional (2D) materials investigation have been one of the most popular and important research field in physics, chemistry and material science. So far, many 2D materials have been proposed, including graphene [3–10], silicene [11, 12], TMDC [13–18], black phosphorus [19–21], h-BN [22–24] *et al.*, and lots of researches have been carried out to investigate their chemical, electronic, optical, mechanical, thermal and magnetic properties [25–32]. These materials span metal, Dirac semiconductor, direct band semiconductor and insulator, and show extensive application prospect in nanoscale electronics and spintronics considering of their natural dimensional constraint and typical material behaviors.

Three-dimensional GeP_3 has been investigated for many years, which are extensively considered to possess a promising application prospect of anode materials because of higher specific capacity compared with those of carbonaceous materials. Using facial and large-scale ball milling method, Qi *et al.* [33] prepared GeP_3/C nanocomposite anode material, which shows excellent lithium storage performance with a high reversible capacity up to 1109 $mA{\cdot}h{\cdot}g^{-1}$ after 130 cycles at a current density of 0.1 $A{\cdot}g^{-1}$. The reversible capacity can sustain with only a little change even at very high current density. Using first principles calculation method, Zhang *et al.* [34] investigated the electric behaviors of the adsorption of Li atoms on single-layer GeP_3. They found that Li-GeP_3 has merits of huge capacity, small diffusion barrier, and low average open-circuit voltages,

which indicates a promising application of this material in rechargeable lithium batteries.

Very recently, 2D GeP_3 with a few layers was theoretically proposed and its structural and electronic behaviors were investigated using first principles calculation method [1]. Similar to black phosphorus, GeP_3 possesses a puckered honeycomb structure, where each germanium atom is enclosed by three phosphorus atoms in an equivalent plane. The authors proved that 2D GeP_3 with few layers is dynamically stable and can exist independently by calculating phonon dispersion spectrum. With the decrease of dimension of GeP_3 from multilayer to monolayer, its electronic behavior transforms from metallic to semiconducting. For a monolayer GeP_3, a low indirect band gap of 0.55 eV appears at the Fermi level. The number of layers induced metal-semiconductor phase transition of GeP_3 indicates a potential application of nanoelectronic devices via building nanoscale tunneling junctions.

So far, no research has been carried out to investigate the quantum transport of GeP_3 nanoribbon based tunneling junctions. Comparing to the conventional tunneling junctions including molecular junctions and bulk tunneling junctions, which have been extensively investigated both theoretically and experimentally [20, 21, 35, 36], nanoribbon based tunneling junctions have several merits. The molecular junctions are extremely hard to control the connecting details because the electric conduction is so sensitive to the connection between the molecule and leads. In comparison, the nanoribbon based junctions can provide a definite quantum transport property. Comparing to the bulk tunneling junctions, the nanoribbon based tunneling junction is boundary control with additional edge characteristics [37–39] and shows more promising usage in the future.

In this paper, we propose several kinds of GeP_3 nanoribbon based tunneling junctions and investigate their electric transport behaviors using first principles calculation method. The density of states (DOS), transmission coefficients and I–V curves were calculated for all the GeP_3 nanoscale tunneling junctions under different bias voltage and gate voltage. We found that the quantum transport behaviors have large distinction among different tunneling junctions. For several tunneling junctions, conductance is large and increases versus gate voltage. While for other tunneling junctions, conductance is small and decreases versus gate voltage. In the following, we introduce the GeP_3 nanoribbon based tunneling junctions and the numerical results in detail.

2 Structures and simulation methods

Figures 1(a)–(c) display three different configurations of hydrogenated zigzag trilayer-monolayer-trilayer GeP_3 nanoribbon based tunneling junctions, where only the bottom layer, the middle layer and the top layer of monolayer nanoribbon in the center region are extended to the bilateral semi-infinite trilayer GeP_3 nanoribbons. These bottom-connecting, middle-connecting and top-connecting tunneling junctions are hereafter named configuration I, configuration II, and configuration III, respectively. In our calculation, the length of central monolayer nanoribbon is changed from $N = 5$ to $N = 11$ and the width is fixed equal to $M = 4$ for each configuration, where N and M are the number of unit length along transverse and transport direction, respectively. All the lateral atoms are saturated by hydrogen atoms and the structures are relaxed using VASP [40] accomplished by PBE functional along with PAW potentials [41, 42]. The kinetic energy cutoff was chosen to be 500 eV and the reciprocal space was meshed by $13 \times 9 \times 1$ using the Monkhorst–Pack method [43]. The volumes of structures were fully relaxed until the atomic force is smaller than 0.001 eV/Å. Numerical results show that the total energy of configurations I and configuration III are more lower than that of configuration II, and the distances between layers are 3.17 Å for the top two layers and 3.64 Å for the bottom two layers. Nanoribbon at each layer is slightly deformed but keeps the same width as the other ones. To see more clearly, the unit cell of the monolayer bottom ribbon, the monolayer middle ribbon, and the monolayer top ribbon are shown individually in Figs. 1(d)–(f). Note that the unit cells of bottom ribbon and middle ribbon are identical, but they are different from that of the top ribbon. For the bottom ribbon and the middle ribbon, the atoms at both zigzag edges are phosphorus, while for the top ribbon the atoms at both zigzag edges are phosphorus and germanium alternatively.

The quantum transport properties of the GeP_3 tunneling junctions were implemented by the transport package Nanodcal, which is based on the standard NEGF-DFT method [44]. In our calculation, norm-conserving non-local pseudo-potential was used to define the atomic cores [45], and atomic orbital basis set with double-ζ plus polarization was used to expand physical quantities [46, 47]. The exchange correlation potential was treated using the LDA functional [42, 48, 49]. Finally, the NEGF-DFT self-consistency was carried out until the numerical tolerance of the Hamiltonian matrix is less than 10^{-4} eV.

3 Numerical results and analysis

In this section, we show our numerical results of electric behavior and quantum transport of the GeP_3 tunneling junctions, including the density of states (DOS), transmission coefficients T and I–V curves. Previous investigation indicated that 2D monolayer GeP_3 shows semi-

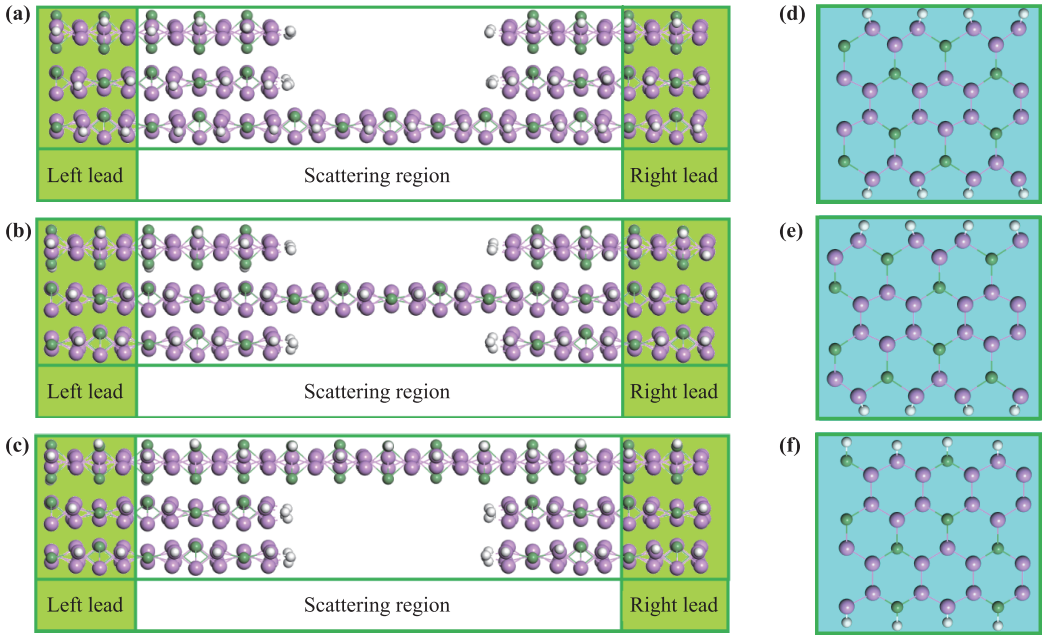

Fig. 1 **(a–c)** Side view of schematic structures of hydrogenated zigzag trilayer-monolayer-trilayer GeP_3 tunneling junctions with $N = 9$ and $M = 4$ for (a) configuration I, (b) configuration II, and (c) configuration III. For each configuration, the trilayer GeP_3 nanoribbon leads are extended to left and right infinity as highlighted by green color. In the center region, only the bottom layer, the middle layer and the top layer of the monolayer nanoribbon is extended to the bilateral trilayer GeP_3 buffer layer respectively for configuration I, configuration II and configuration III. **(d–f)** Top view of the periodic structures of (d) bottom layer, (e) middle layer, and (f) top layer of hydrogenated zigzag GeP_3 lead. The purple, green and white balls indicate phosphorus, germanium and hydrogen atoms, respectively. For the bottom ribbon and the middle ribbon, the atoms at both zigzag edges are phosphorus, while for the top ribbon the atoms at both zigzag edges are phosphorus and germanium alternatively.

conducting behavior, while few layers GeP_3 is transformed to be conducting. Therefore, we want to first analyze the electronic behavior of different GeP_3 nanoribbon as shown in Figs. 1(d)–(f). Figures 2(a)–(c) show DOS of isolated GeP_3 monolayer bottom ribbon (the same as the monolayer middle ribbon), monolayer top ribbon, and trilayer ribbon of leads, respectively, by projecting the DOS to the s orbitals and p orbitals of phosphorus and germanium. Several information can be found: (i) both monolayer bottom ribbon and monolayer top ribbon show semi-conducting behavior, and the gap of the former is smaller than that of the latter. This is mainly caused by the chemical inequivalence of the edge atoms between the monolayer GeP_3 nanoribbon. According to Ref. [50], the band structure near the Fermi level of a nanoribbon is mainly dominated by edge atoms, and band gap increases versus chemical inequivalence of these edge atoms. For the bottom ribbon as shown in Fig. 1(d), one zigzag edge is upfolded, while the other is downfolded, indicating the two zigzag edges composed of P atoms are inequivalent. However, for the top ribbon as shown in Fig. 1(f), P atoms and Ge atoms are interphase at both sides with a Ge (P) atom at one edge corresponding to a P (Ge) atom at the other edge. Besides the folding inequivalence of atoms at both zigzag edges, the positions of Ge and P atoms at both zigzag edges are also inequivalent. Thus the chemical inequivalence of the top ribbon is more obvious than that of the bottom ribbon, and therefore a larger gap for the latter. In other words, the appearance of lateral Germanium atoms increases the CBM and decreases the VBM of the monolayer top ribbon comparing to the monolayer bottom nanoribbon. (ii) For both monolayer nanoribbons, the CBM and the VBM are mainly contributed by p orbitals of phosphorus atoms, and then contributed by p orbitals of germanium atoms. The contribution from s orbitals of phosphorus and germanium atom is much smaller. This behavior of PDOS of monolayer GeP_3 nanoribbon is very close to that of 2D monolayer GeP_3 found in Ref. [1]. (iii) Different from the monolayer ribbons, trilayer GeP_3 ribbon shows metallic behavior, where all the orbitals of phosphorus and germanium near the Fermi level are spread enormously and overlap at the Fermi level. To see more clearly, Fig. 2(d) shows the PDOS of trilayer GeP_3, where DOS is projected to each layer of trilayer GeP_3 nanoribbon. Comparing to monolayer GeP_3 nanoribbon, each layer of trilayer GeP_3 ribbon is transformed from semi-conducting to metallic due to the interaction between layers.

In the following, we analyze the transmission coeffi-

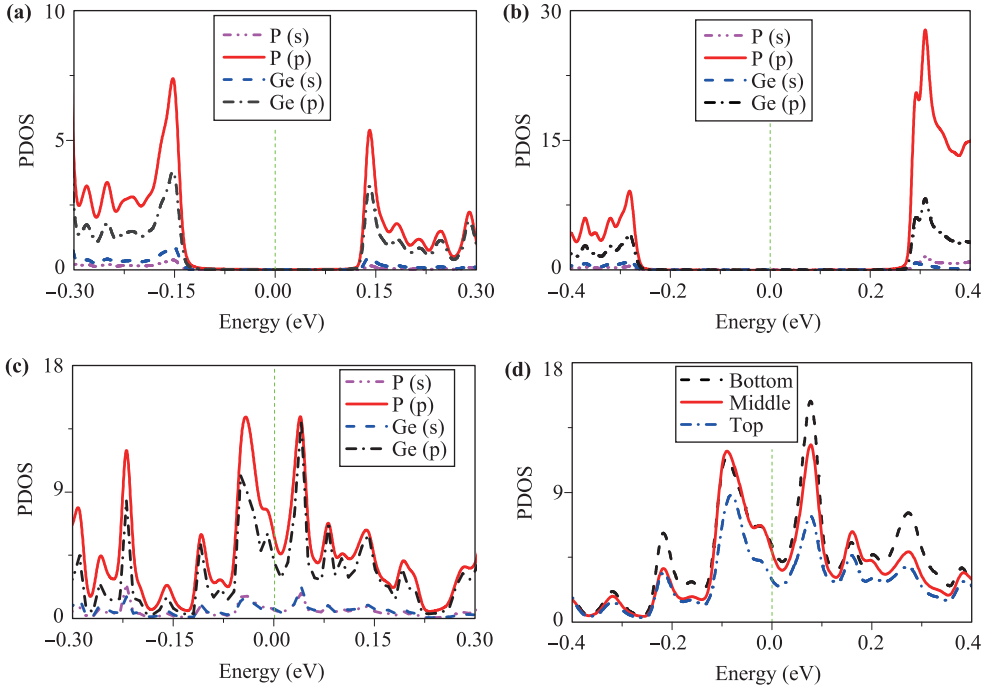

Fig. 2 **(a–c)** PDOS of periodic zigzag GeP_3 nanoribbon for (a) monolayer bottom ribbon; (b) monolayer top ribbon; and (c) trilayer ribbon of leads. In each panel, the pink dash-dot-dot curves, red solid curves, blue dash curves, and black dash-dot curves indicate the DOS projected to s orbitals of phosphorus, p orbitals of phosphorus, s orbitals of germanium, and p orbitals of germanium. The vertical green dash lines are the Fermi level. **(d)** PDOS of trilayer GeP_3 versus energy projected to the bottom ribbon, the middle ribbon and the top ribbon.

cient of different configurations of GeP_3 tunneling junctions. The transmission coefficient T of a two probe system can be calculated by [51]

$$T(E) = 4\mathrm{Tr}[\mathrm{Im}(\Sigma_L(E))G^r(E)\mathrm{Im}(\Sigma_R(E))G^a(E)], \quad (1)$$

where $\Sigma_{L/R}$ is the self-energy which describes the coupling between lead L/R and scattering region; $G^{r,a}$ is the retarded/advanced Green's function of the system, which is defined as $G^r = [G^a]^\dagger = [E - H - \Sigma_L - \Sigma_R]^{-1}$ with H the Hamiltonian of system. Fig. 3(a) shows T versus E of GeP_3 tunneling junctions with bias voltage equal to zero, where the black solid curve, red dash curve and blue dash-dot curve are for configuration I, configuration II, and configuration III, respectively. We can find that the transmission coefficient at the Fermi level $T(E_F)$ is largest for configuration I (roughly equal to 0.2), and is least for configuration III (roughly equal to 0.001). The magnitude of $T(E_F)$ of configuration II is in the middle and roughly equal to 0.01. Besides, there are several broad peaks of $T(E)$ above the Fermi level for configuration I and II, while the peaks disappear for configuration III. Considering of the different configuration as shown in Fig. 1, we can draw a conclusion that the difference of $T(E)$ between configuration I and configuration II is contributed by the different connecting potential between the scattering region and leads, i.e., the bottom-connecting and middle-connecting potentials. As shown in Figs. 1(d), (e) and (f), the structures of the middle layer and the bottom layer of nanoribbon are the same, and they are different from the top layer. That means the only difference between configuration I and configuration II is the connecting formation between the trilayer ribbon (leads) and the monlayer ribbon (center). In other words, the difference of $T(E)$ between configuration I and configuration II is contributed by the different connecting potential between the monolayer ribbon and the buffer layers in the scattering region. While the difference of $T(E)$ between configuration I and configuration III is mainly due to the different structure of monolayer GeP_3 nanoribbon in the scattering region, i.e., the ribbon edges with pure phosphorus and phosphorus/germanium alternatively. Because the band gap of monolayer top ribbon is much larger than that of bottom ribbon, the barrier in configuration III is much higher than that in configuration I, and therefore $T(E_F)$ of configuration III is much smaller than that of configuration I.

Furthermore, we found that the peak of $T(E)$ at $E = 0.045$ eV for configuration I is mainly contributed by the trilayer GeP_3 nanoribbons leads whose DOS shows a peak at roughly the same energy as shown in Fig. 2(c). Although the section of monolayer bottom ribbon in the central of scattering region shows semi-conducting be-

havior at $E = 0.045$ eV, its barrier height is not large enough to block the overlap of expending p states of left lead and right lead in the center region for configuration I, and therefore a large peak of $T(E)$ appears. While for configuration III, the continuum states of left lead and right lead at roughly $E = 0.045$ eV are blocked in left and right region, respectively, by the central monolayer top ribbon due to its high potential barrier. As a result, $T(E)$ near $E = 0.045$ eV is very small for configuration III, although DOS of both leads near this energy are very large. To see more intuitively, we plot the real space scattering DOS at $E = 0.045$ eV in Figs. 3(b)–(d) for configuration I–III, respectively. Obviously, the scattering DOS of both leads are largely overlapped in the center region for configuration I, slightly overlapped for configuration II, and barely overlapped for configuration III, corresponding to the decrease of transmission coefficient in sequence. The other peaks of $T(E)$ above the Fermi level in Fig. 3(a) can be understood similarly.

Next, we analysis the influence of gate voltage to transmission coefficient for each configuration. In our numerical calculation, the gate voltage is simulated by supplying a uniform electric field to the central monolayer nanoribbon along the vertical direction. Finally, the gate controlled hamiltonian of the system can be determined self-consistently using first-principles calculations by ensuring the continuous and derivative continuous of charge and potential at the gate boundaries. Figures 4(a)–(c) show the conductances G versus gate voltage V_g from -5 V to 5 V for configuration I, II, and III, respectively. For configuration I and II, the conductance increases versus gate voltage, which implies an n-type conduction. While for configuration III, the conductance decrease versus gate voltage, where a p-type conduction is performed. To understand these behaviors, we calculated the scattering states at the Fermi level of each configuration under different voltage, and then projected these states to the renormalized energy levels of the scattering region using the following equation,

$$P_O = |\langle \phi_O | \Psi(E_F) \rangle|^2, \tag{2}$$

where ϕ_O is the renormalized LUMO or HOMO of monolayer GeP_3 nanoribbon section in the central of scattering region including the influence from leads, and $\Psi(E_F)$ represents the scattering state at the Fermi level of each configuration under different gate voltage. Numerical results are shown in Figs. 4(d)–(f), where P_{LUMO} and P_{HOMO} under zero and 5 V gate voltages are plotted for configuration I, II, and III, respectively. We found that although $T(E_F)$ is small for each configuration, it is still mainly contributed by the renormalized LUMO and HOMO states, indicating the validity of this method in conductance analysis. For configuration I and II, LUMO levels are closer to the Fermi level than HOMO levels when V_g is equal to zero, and therefore P_{LUMO} is larger than P_{HOMO}. With increasing of gate voltage, the LUMO

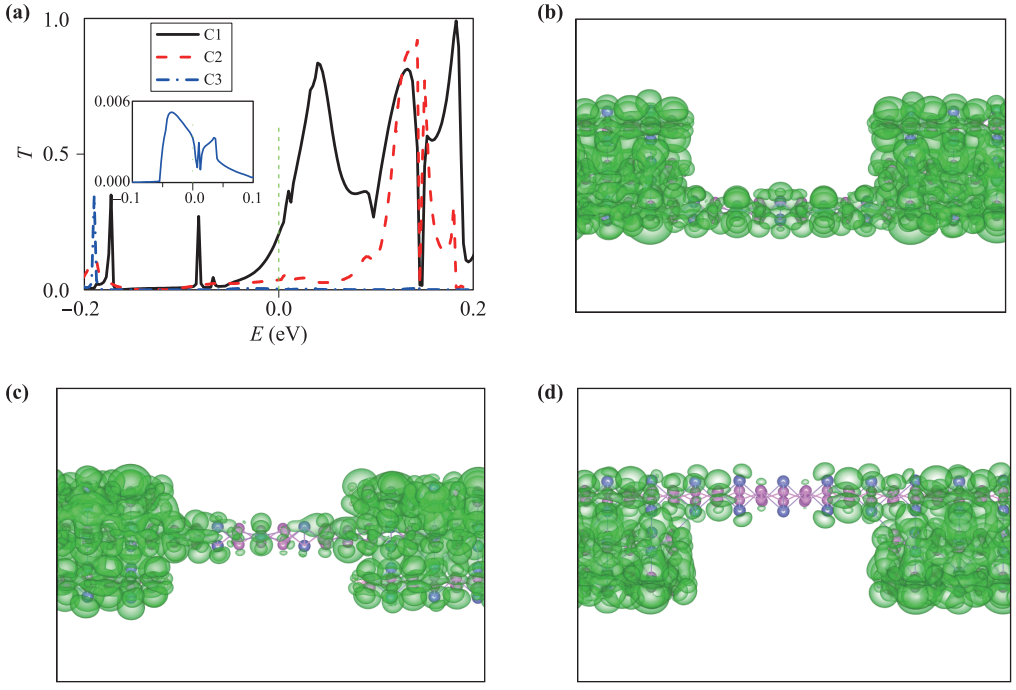

Fig. 3 **(a)** $T(E)$ versus E under zero bias voltage for configuration I (C1), configuration II (C2), and configuration III (C3) with $N = 9$. The vertical green dash line indicates the Fermi level. Inset: Detail view of $T(E)$ near the Fermi level for configuration III. **(b–d)** Isosurface plot of real space distribution of scattering states at $E = 0.045$ eV for configuration I-III with $N = 9$, respectively, where the value of isosurface plot is 4×10^{-6}.

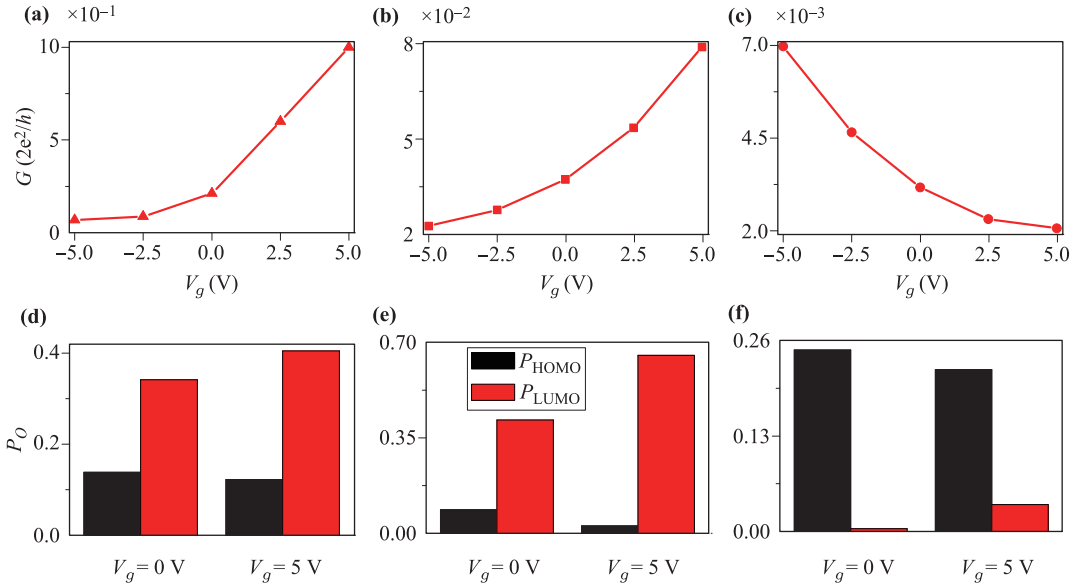

Fig. 4 **(a–c)** G versus V_g for (a) configuration I with $N = 9$, (b) configuration II with $N = 9$, and (c) configuration III with $N = 9$. **(d–f)** Normalized P_{HOMO} and P_{LUMO} under different gate voltages for configuration I, II, III, respectively.

level is pushed closer to the Fermi level accompanied with increasing P_{LUMO}. As a result, $T(E_F)$ increases as a function of gate voltage as shown in Figs. 4(a)–(b). While for configuration III, HOMO level is closer to the Fermi level than LUMO level when V_g is equal to zero, and $T(E_F)$ is mainly dominated by P_{HOMO}. With increasing of gate voltage, the HOMO level is pushed away from the Fermi level, and therefore $T(E_F)$ decreases.

Figures 5(a)–(c) show equilibrium $T(E)$ as a function of energy for configuration I, II, and III, respectively, with different length N ($N = 5$, 7, 9, 11). For each configuration, $T(E_F)$ decreases with increasing of N. This is reasonable because the height of potential barrier in the middle central is proportional to the length of central semiconducting GeP_3 monolayer nanoribbon. Figures 5(d)–(f) show the conductance G versus N for each configuration, respectively, where $G = 2e^2/hT(E_F)$. We found G show roughly exponential decay versus N for each configuration by $G = G_0 e^{-\beta N}$, where the decay factors β of configuration I, II, and III were fitted and equal to be 0.4967, 0.6459, and 0.9097, respectively. Obviously, the decay rate of configuration I is much smaller than configuration III.

Finally, the non-equilibrium transport behaviors were investigated for each configuration, where the electric currents of each configuration was calculated using the Landauer-Büttiker formula as follows [52]:

$$I = -\frac{e}{h}\int_{-\infty}^{+\infty} \mathrm{d}E[f_L(E-\mu_L) - f_R(E-\mu_R)]T(E), \quad (3)$$

where $f_{L/R}$ is the Fermi distribution function of left/right lead. Figure 6 shows the I–V curve for each configuration under different gate voltages. For configuration I and II, currents increase versus bias voltage roughly linearly under different gate voltage. For a given bias voltage, current increases with gate voltage due to the increase of transmission coefficient as shown in Figs. 4(a)–(b). While for configuration III, negative differential resistance appears when bias voltage is roughly larger than 0.05 V and smaller than −0.05 V. By comparing the transmission coefficients under different bias voltage, we found that a sharp peak of $T(E)$ in the integral energy domain of Eq. (3) is leveled with further increasing or decreasing of bias voltage, although the integral energy domain of $T(E)$ is increased. Currents decrease in sequence from configuration I to configuration III for the structures with the same center length, showing accordant behavior of transmission coefficient as shown in Fig. 3(a). Moreover, we found that the influence of gate voltage to a short structure is smaller than to a long structure as shown in Figs. 6(a) and (d). This is reasonable because the contribution from both leads to $T(E)$ is more affected by a gate voltage for a short structure.

4 Summary

In summary, we propose a first-principles calculation to investigate the quantum transport properties of several GeP_3 nanoribbon based atomic tunneling junctions. Numerical results indicate that monolayer GeP_3 nanoribbon shows semiconducting behavior, while trilayer GeP_3 nanoribbon expresses metallic behavior due to the strong interaction between each of the layers.

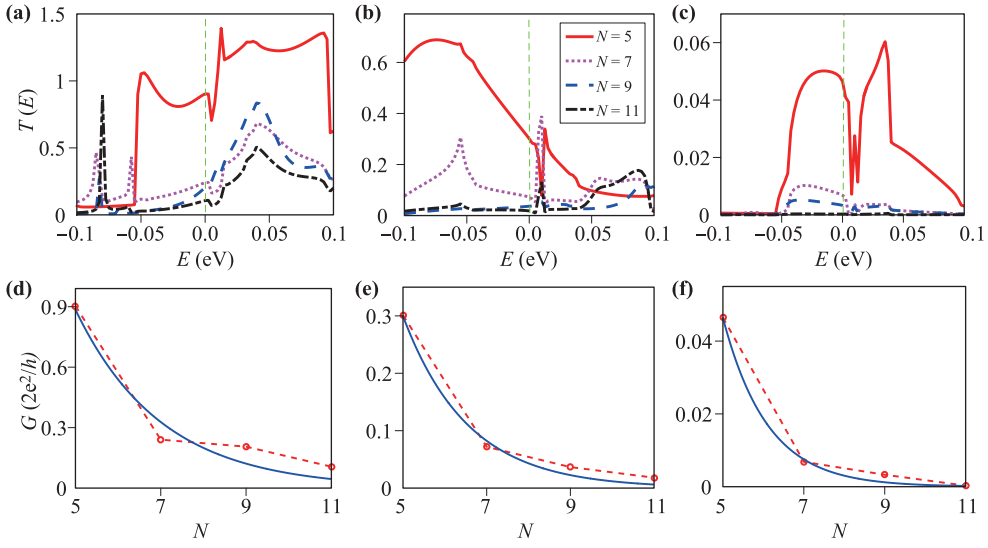

Fig. 5 **(a–c)** $T(E)$ versus E for (a) configuration I with different N, (b) configuration II with different N, and (c) configuration III with different N. The vertical green dash lines indicate the Fermi level. **(d–f)** G versus N with $V_g = 0$ for (d) configuration I, (e) configuration II, and (f) configuration III. The circle-dash curves are from the first principles calculation, and the solid curves are from the simulation. The simulated decay factor A is equal to 0.4967, 0.6459, and 0.9097 for configuration I, II, and III, respectively.

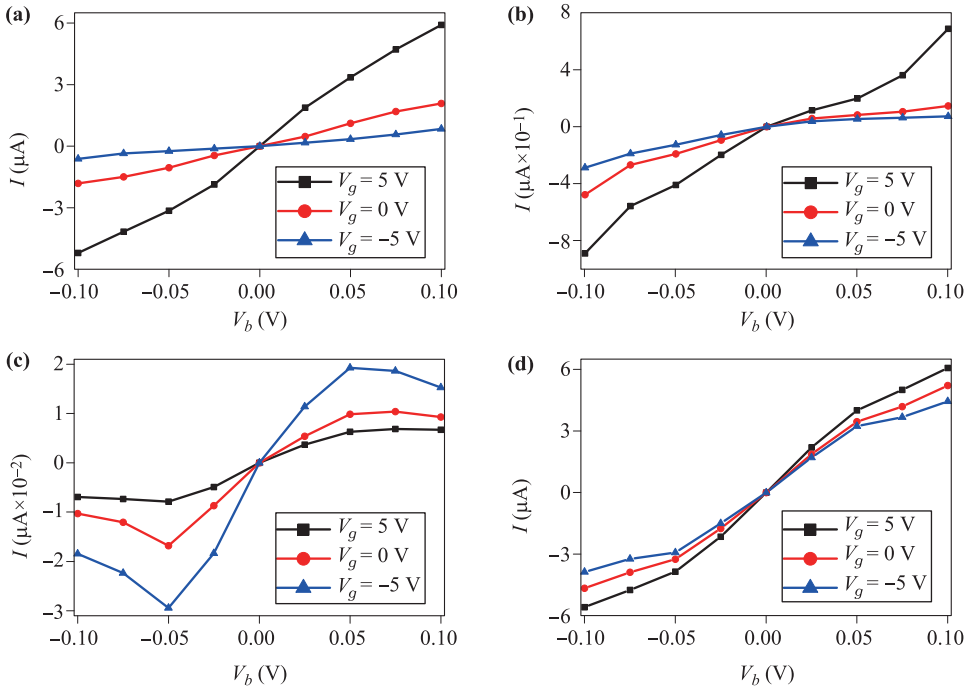

Fig. 6 I–V curves under different gate voltage for **(a)** configuration I with $N = 9$, **(b)** configuration II with $N = 9$, **(c)** configuration III with $N = 9$, and **(d)** configuration I with $N = 5$.

This behavior is accordant with that proposed in two dimensional GeP_3 layers. The transmission coefficient $T(E)$ of tunneling junctions is sensitive to the connecting formation between the central monolayer GeP_3 nanoribbon and the trilayer GeP_3 nanoribbon at both ends. $T(E)$ of the bottom-connecting tunneling junction is much larger than that of the middle-connecting and top-connecting ones. With increase of gate voltage, the conductances increases for the bottom-connecting and middle-connecting tunneling junctions, while de-

creases for the top-connecting tunneling junctions. In addition, the conductance decreases exponentially versus the length of central monolayer GeP_3 nanoribbon for all the tunneling junctions. I–V curves show roughly linear behavior for the bottom-connecting and middle-connecting structures, while exhibit negative differential resistance for the top-connecting structures. These properties offer GeP_3 an interesting new employment in device applications for both nano-scale probes and semiconductors.

Acknowledgements This work was financially supported by grants from the National Natural Science Foundation of China (Grant No. 11774238) and Shanxi 1331KSC.

References

1. Y. Jing, Y. Ma, Y. Li, and T. Heine, GeP_3: A small indirect band gap 2D crystal with high carrier mobility and strong interlayer quantum confinement, *Nano Lett.* 17(3), 1833 (2017)
2. K. S. Novoselov, A. K. Geim, S. V. Morozov, D. Jiang, Y. Zhang, S. V. Dubonos, I. V. Grigorieva, and A. A. Firsov, Electric field effect in atomically thin carbon films, *Science* 306(5696), 666 (2004)
3. S. Z. Butler, S. M. Hollen, L. Cao, Y. Cui, J. A. Gupta, H. R. Gutiérrez, T. F. Heinz, S. S. Hong, J. Huang, A. F. Ismach, E. Johnston-Halperin, M. Kuno, V. V. Plashnitsa, R. D. Robinson, R. S. Ruoff, S. Salahuddin, J. Shan, L. Shi, M. G. Spencer, M. Terrones, W. Windl, and J. E. Goldberger, Progress, challenges, and opportunities in two-dimensional materials beyond graphene, *ACS Nano* 7(4), 2898 (2013)
4. F. Bonaccorso, L. Colombo, G. Yu, M. Stoller, V. Tozzini, A. C. Ferrari, R. S. Ruoff, and V. Pellegrini, Graphene, related two-dimensional crystals, and hybrid systems for energy conversion and storage, *Science* 347(6217), 1246501 (2015)
5. S. D. Sarma and S. Adam, E. H. wang and E. Rossi, Electronic transport in two-dimensional graphene, *Rev. Mod. Phys.* 83(407), 407 (2011)
6. A. H. N. Castro, F. Guinea, N. M. R. Peres, K. S. Novoselov, and A. K. Geim, The electronic properties of graphene, *Rev. Mod. Phys.* 81(109), 109 (2009)
7. A. Lherbier, X. Blase, Y. M. Niquet, F. Triozon, and S. Roche, Charge transport in chemically doped 2D graphene, *Phys. Rev. Lett.* 101(3), 036808 (2008)
8. B. Z. Rameshti and A. G. Moghaddam, Spin-dependent Seebeck effect and spin caloritronics in magnetic graphene, *Phys. Rev. B* 91(15), 155407 (2015)
9. Y. Xing, Q. Sun, and J. Wang, Nernst and Seebeck effects in a graphene nanoribbon, *Phys. Rev. B* 80(23), 235411 (2009)
10. B. Wang, J. Li, F. Xu, Y. Wei, J. Wang, and H. Guo, Transient dynamics of magnetic Co-graphene systems, *Nanoscale* 7(22), 10030 (2015)
11. A. Fleurence, R. Friedlein, T. Ozaki, H. Kawai, Y. Wang, and Y. Takamura, Experimental evidence for epitaxial silicene on diboride thin films, *Phys. Rev. Lett.* 108(24), 245501 (2012)
12. P. Vogt, P. D. Padova, C. Quaresima, J. Avila, E. Frantzeskakis, M. C. Asensio, A. Resta, B. Ealet, and G. L. Lay, Silicene: compelling experimental evidence for Graphene like two-dimensional silicon, *Phys. Rev. Lett.* 108(15), 155501 (2012)
13. A. Subedi, L. Zhang, D. J. Singh, and M. H. Du, Density functional study of FeS, FeSe, and FeTe: Electronic structure, magnetism, phonons, and superconductivity, *Phys. Rev. B* 78(13) (2008)
14. D. Xiao, G. B. Liu, W. Feng, X. Xu and W. Yao, Coupled spin and valley physics in monolayers of MoS_2 and other group-VI dichalcogenides, *Phys. Rev. Lett.* 108, 196802 (2012)
15. M. Ramakrishna, A. Gomathi, A. K. Manna, D. J. Late, R. Datta, S. K. Pati, and C. N. R. Rao, MoS_2 and WS_2 analogues of graphene, *Angew. Chem. Int. Ed.* 49(24), 4059 (2010)
16. K. F. Mak, C. Lee, J. Hone, J. Shan, and T. F. Heinz, Atomically thin MoS_2: A new direct-gap semiconductor, *Phys. Rev. Lett.* 105(13), 136805 (2010)
17. Q. H. Wang, K. Kalantar-Zadeh, A. Kis, J. N. Coleman, and M. S. Strano, Electronics and optoelectronics of two-dimensional transition metal dichalcogenides, *Nat. Nanotechnol.* 7(11), 699 (2012)
18. L. Zhang, L. Wan, Y. Yu, B. Wang, F. Xu, Y. Wei, and Y. Zhao, Modulation of electronic structure of armchair MoS_2 nanoribbon, *J. Phys. Chem. C* 119(38), 22164 (2015)
19. F. Xia, H. Wang, and Y. Jia, Rediscovering black phosphorus as an anisotropic layered material for optoelectronics and electronics, *Nat. Commun.* 5, 4458 (2008)
20. L. Li, Y. Yu, G. J. Ye, Q. Ge, X. Ou, H. Wu, D. Feng, X. H. Chen, and Y. Zhang, Black phosphorus field-effect transistors, *Nat. Nanotechnol.* 9(5), 372 (2014)
21. H. Liu, A. T. Neal, Z. Zhu, Z. Luo, X. Xu, D. Tomanek, and P. D. Ye, Phosphorene: An unexplored 2D semiconductor with a high hole mobility, *ACS Nano* 8(4), 4033 (2014)
22. C. Y. Zhi, Y. Bando, C. C. Tang, H. Kuwahara, and D. Golberg, Large-scale fabrication of boron nitride nanosheets and their utilization in polymeric composites with improved thermal and mechanical properties, *Adv. Mater.* 21(28), 2889 (2009)
23. J. H. Warner, M. H. Rümmeli, A. Bachmatiuk, and B. Büchner, Atomic resolution imaging and topography of boron nitride sheets produced by chemical exfoliation, *ACS Nano* 4(3), 1299 (2010)

24. A. Nag, K. Raidongia, K. P. S. S. Hembram, R. Datta, U. V. Waghmare, and C. N. R. Rao, Graphene analogues of BN: Novel synthesis and properties, *ACS Nano* 4(3), 1539 (2010)
25. P. Miró, M. Audiffred, and T. Heine, An atlas of two-dimensional materials, *Chem. Soc. Rev.* 43(18), 6537 (2014)
26. C. L. Haynes and R. P. Van Duyne, Nanosphere lithography: A versatile nanofabrication tool for studies of size dependent nanoparticle optics, *J. Phys. Chem. B* 105(24), 5599 (2001)
27. J. C. Knight, J. Broeng, T. A. Birks, and P. S. J. Russel, Photonic band cap guidance in optical fibers, *Science* 282(5393), 1476 (1998)
28. A. V. Krasheninnikov, and K. Nordlund, Ion and electron irradiation-induced effects in nanostructured materials, *J. Appl. Phys.* 107(7), 071301 (2010)
29. Z. H. Qiao, S. A. Yang, B. Wang, Y. G. Yao, and Q. Niu, Spin-polarized and valley helical edge modes in graphene nanoribbons, *Phys. Rev. B* 84(3), 035431 (2011)
30. B. Wang and J. Wang, First-principles investigation of transport properties through longitudinal unzipped carbon nanotubes, *Phys. Rev. B* 81(4), 045425 (2010)
31. W. Rechberger, A. Hohenau, A. Leitner, J. R. Krenn, B. Lamprecht, and F. R. Aussenegg, Optical properties of two interacting gold nanoparticles, *Opt. Commun.* 220(1–3), 137 (2003)
32. D. Xiao, G. B. Liu, W. Feng, X. Xu, and W. Yao, Coupled spin and valley physics in monolayers of MoS_2 and other group-VI dichalcogenides, *Phys. Rev. Lett.* 108(19), 196802 (2012)
33. W. Qi, H. Zhao, Y. Wu, H. Zeng, T. Tao, C. Chen, C. Kuang, S. Zhou, and Y. Huang, Facile synthesis of layer structured GeP_3/C with stable chemical bonding for enhanced lithium-ion storage, *Sci. Rep.* 7, 43582 (2017)
34. C. Zhang, Y. Jiao, T. He, F. Ma, L. Kou, T. Liao, S. Bottle, and A. Du, Two-dimensional GeP_3 as a high capacity electrode material for Li-ion batteries, *Phys. Chem. Chem. Phys.* 19(38), 25886 (2017)
35. W. X. Lai, C. Zhang, and Z. S. Ma, Single molecular shuttle junction: Shot noise and decoherence, *Front. Phys.* 10(1), 108501 (2015)
36. Z. Y. Ning, J. S. Qiao, W. Ji, and H. Guo, Correlation of interfacial bonding mechanism and equilibrium conductance of molecular junctions, *Front. Phys.* 9(6), 780 (2014)
37. Y. Cai, G. Zhang, and Y. W. Zhang, Polarity-reversed robust carrier mobility in monolayer MoS_2 nanoribbons, *J. Am. Chem. Soc.* 136(17), 6269 (2014)
38. Y. Zhang, X. H. Yan, Y. D. Guo, and Y. Xiao, Magnetization distribution and spin transport of graphene/h-BN/graphene nanoribbon-based magnetic tunnel junction, *Phys. Lett. A* 381(35), 2949 (2017)
39. J. W. Li, B. Wang, Y. J. Yu, Y. D. Wei, Z. Z. Yu, and Y. Wang, Spin-resolved quantum transport in graphene-based nanojunctions, *Front. Phys.* 12(4) (2016)
40. G. Kresse and J. Furthmuller, Efficient iterative schemes for ab initio total-energy calculations using a plane-wave basis set, *Phys. Rev. B* 54(16), 11169 (1996)
41. P. E. Blöchl, Projector augmented-wave method, *Phys. Rev. B* 50(24), 17953 (1994)
42. J. P. Perdew, A. Ruzsinszky, G. I. Csonka, O. A. Vydrov, G. E. Scuseria, L. A. Constantin, X. Zhou, and K. Burke, Restoring the density-gradient expansion for exchange in solids and surfaces, *Phys. Rev. Lett.* 100(13), 136406 (2008)
43. H. J. Monkhorst and J. D. Pack, Special points for Brillouin zone integrations, *Phys. Rev. B* 13(12), 5188 (1976)
44. J. Taylor, H. Guo, and J. Wang, Ab initio modeling of quantum transport properties of molecular electronic devices, *Phys. Rev. B* 63(24), 245407 (2001)
45. D. Hamann, M. Schlüter, and C. Chiang, Norm-conserving pseudopotentials, *Phys. Rev. Lett.* 43(20), 1494 (1979)
46. P. Ordejón, E. Artacho, and J. M. Soler, Self-consistent order-N density-functional calculations for very large systems, *Phys. Rev. B* 53(16), R10441 (1996)
47. J. M. Soler, E. Artacho, J. D. Gale, A. García, J. Junquera, P. Ordejón, and D. Sánchez-Portal, The SIESTA method for ab initio order-N materials simulation, *J. Phys.: Condens. Matter* 14(11), 2745 (2002)
48. E. J. Meijer and M. Sprik, A density-functional study of the intermolecular interactions of benzene, *J. Chem. Phys.* 105(19), 8684 (1996)
49. S. Goedecker and C. Umrigar, Critical assessment of the self-interaction corrected local density functional method and its algorithmic implementation, *Phys. Rev. A* 55(3), 1765 (1997)
50. G. Giovannetti, P. A. Khomyakov, G. Brocks, P. J. Kelly, and J. van den Brink, Substrate-induced band gap in graphene on hexagonal boron nitride: Ab initio density functional calculations, *Phys. Rev. B* 76(7), 073103 (2007)
51. B. G. Wang, J. Wang, and H. Guo, Nonlinear spin polarized transport through a ferromagnetic nonmagnetic ferromagnetic junction, *J. Phys. Soc. Jpn.* 70(9), 2645 (2001)
52. M. Büttiker, Y. Imry, R. Landauer, and S. Pinhas, Generalized many-channel conductance formula with application to small rings, *Phys. Rev. B* 31(10), 6207 (1985)